

X-ray spectral and timing evolution during the 2018 outburst of MAXI J1820+070

YaXing Li^{1,2}, Zhen Yan^{1*}, ChenXu Gao^{1,2}, and Wenfei Yu¹

¹Shanghai Astronomical Observatory, Chinese Academy of Sciences, 80 Nandan Road, Shanghai 200030, China

²University of Chinese Academy of Sciences, 19A Yuquan Road, Beijing 100049, China

Accepted XXX. Received YYY; in original form ZZZ

ABSTRACT

We made use high-cadence observations from the *Insight*-HXMT and *NICER* to scrutinize the spectral and timing evolution during the 2018 outburst of the black hole X-ray binary (BHXR) MAXI J1820+070. Its hardness-intensity diagram (HID) displays a “q”-like track including all the spectral states, along a unique loop in the hard state. The tracks observed in the HID is anticipated in the evolution of the components responsible for Compton and reflection emission. This is substantiated by the relationship between the X-ray luminosity L_X and photon index Γ , as well as the relationship between X-ray luminosity L_X and the ratio of Compton to disk luminosities L_C/L_D . Both of these relationships exhibit a pattern reminiscent of HID. During the hard state, the hardness (also Γ) is determined by either reflection component ($R_f > 1$) or Compton component ($R_f < 1$) depending on the value reflection fraction R_f . So the distinctive evolution of R_f leads to the unique loop in the HID (also in the L_X – Γ plane) of hard state. Additionally, we found a negative correlation between frequency of the type-C quasi-periodic oscillation (QPO) ($\nu_{C,QPO}$) and the optical depth of the Compton emission (τ), and a positive correlation between $\nu_{C,QPO}$ and Γ . These correlations strongly suggest a coupling between the QPO properties and the underlying process responsible for Comptonization.

Key words: accretion, accretion discs – black hole physics – X-rays: binaries – stars: individual: MAXI J1820+070

1 INTRODUCTION

The majority of Galactic black hole X-ray binaries (BHXR) behave as transient sources that spend years to decades in a quiescent state. Occasionally, they undergo outbursts lasting for weeks to months before returning to quiescence (Yan & Yu 2015; Corral-Santana et al. 2016). These outbursts may involve transitions through distinct accretion states, which are characterized by a variety of X-ray spectral and timing features, along with associated radio emission (see reviews by Remillard & McClintock 2006; Done et al. 2007; Belloni 2010). Given their proximity at kiloparsec distances and their dramatic variability on timescales spanning from days to months, BHXR) serve as excellent targets for real-time monitoring the accretion flow and jet behavior. The high-cadence observations yield valuable insights into the physics of accretion and its interplay with jet across different accretion states.

The outburst usually starts from the hard state (HS) when the luminosity is low. The X-ray spectrum of HS is dominated by Comptonized emission produced from a hot plasma usually called corona (Sunyaev & Truemper 1979), a weak thermal component from the accretion disk is also detected. In this state, the strong low-frequency quasi-periodic oscillations (LFQPOs) and broad line noises (BLNs) are usually detected in the power density spectrum (PDS, e.g. Belloni et al. 2002; Casella et al. 2004). As the outburst goes on, the

disk component becomes stronger. When the spectra is dominated by the thermal component from an optically thick disk extending to the innermost stable circular orbit (ISCO) of the BH (Novikov & Thorne 1973; Shakura & Sunyaev 1973), the outburst enters the soft state (SS). In contrast to HS, SS shows low X-ray variability amplitude with a few percent fractional root mean square (RMS), and LFQPOs are rarely detected (Motta et al. 2012). The transition between the HS and SS is called intermediate state (IMS). During the outburst decay, the disk temperature and luminosity decrease. At some point, the corona restrengthens and dominates over the disk component, which indicates the outburst return to HS.

A large fraction of outbursts experience a transition from the HS to SS state (H-S) during the outburst rise, and conversely, from SS to HS (S-H) during the outburst decay (e.g. Yu & Yan 2009; Tetarenko et al. 2016). Through the comprehensive X-ray spectral and timing analysis, we can conduct detailed research on different spectral states and state transitions (e.g. Belloni 2010). The characteristics extracted from X-ray spectral-timing data reveal the properties and evolution of the accretion flow across different spectral states (e.g. Kara et al. 2019; Fabian et al. 2020; Ma et al. 2021; You et al. 2023a). Notably, the X-ray spectral and timing properties exhibit pronounced changes during these state transitions, providing valuable insights into the changes in innermost accretion flow and/or ejection around the BH.

* E-mail: zyan@shao.ac.cn

2 MAXI J1820+070

In this work, we focus on the evolution of the very bright outburst of MAXI J1820+070. The X-ray outburst MAXI J1820+070 was first detected by Monitor of All-sky X-ray Image (MAXI) on March 11, 2018 (MJD 58188, Kawamuro et al. 2018). The optical counterpart ASASSN-18ey was discovered by the All-Sky Automated Survey for Supernovae (ASAS-SN) (Shappee et al. 2014) around several days earlier (Tucker et al. 2018; Denisenko 2018). Soon after, the source was classified as a BHXRB according to the follow-up observations in different wavelengths (Baglio et al. 2018; Bright et al. 2018; Uttley et al. 2018). Atri et al. (2020) measured the distance of 2.96 ± 0.33 kpc by using the radio parallax method and a jet inclination angle of $63 \pm 3^\circ$ with very long baseline interferometry (VLBI) observations. Torres et al. (2020) estimated the mass of black hole is $8.48^{+0.79}_{-0.72} M_\odot$. The spin of the BH was estimated as 0.14 (Zhao et al. 2021).

Like other transient BHXRBs, MAXI J1820+070 is in HS at the beginning of the outburst. It is a very long HS, extending until around MJD 58290. Subsequently, the source enters the IMS. The above two periods are referred to as rising HS and IMS states. The transient jet ejected around MJD 58306 (Bright et al. 2020; Wood et al. 2021), coinciding with the transition between hard intermediate state (HIMS) and soft intermediate state (SIMS; Fender et al. 2004). The SS lasts from MJD 58310 to 58383. At about MJD 58393, the source returns to the HS. In order to distinguish from the outburst rise phase, the period between MJD 58383 to 58393 and after are referred to as decaying IMS and HS states, respectively. The time intervals of different spectral states are shown in Figure 1 (see also Shidatsu et al. 2019).

Due to its high X-ray brightness (see the public lightcurve in Sakamoto et al. 2016) and low interstellar absorption/extinction (Uttley et al. 2018), MAXI J1820+070 serves as an ideal source for studying outburst evolution across multiple wavelengths. Extensive multi-wavelength campaigns, involving various X-ray missions, have been conducted. By concurrently applying X-ray spectral and timing analysis during this outburst, it is very helpful to uncover the properties and evolution of accretion flows around black holes (e.g. Stiele & Kong 2020; Wang et al. 2020; You et al. 2021). *Insight*-Hard X-ray Modulation Telescope (HXMT) is one of the best missions for performing X-ray spectral and timing study in a very broad energy band 1–250 keV (Zhang et al. 2020). It carries three slat-collimated payloads: low energy X-ray telescope (LE, 1–15 keV, Chen et al. 2020), medium energy X-ray telescope (ME, 5–30 keV, Cao et al. 2020) and high energy X-ray telescope (HE, 20–250 keV, Liu et al. 2020). All three instruments have large collecting areas and high time resolution, which are beneficial to do X-ray spectral and timing analysis for bright targets. *Insight*-HXMT observed MAXI J1820+070 from March 14, 2018 to October 21, 2018, and obtained a total of more than 310 exposures with an average interval of 0.63 days. The *Insight*-HXMT observations extensively cover the different spectral states through almost the entire outburst Figure 1. We also used the data from Neutron Star Interior Composition Explorer (*NICER*) in some cases. Due to its high time resolution and large effective area, *NICER* data can provide X-ray spectral and timing analysis in the 0.2–12 keV.

3 DATA REDUCTION AND DATA ANALYSIS

3.1 *Insight*-HXMT data reduction

The *Insight*-HXMT data and products were processed and extracted by using the *Insight*-HXMT Data Analysis Software package

(HXMTDAS). We first screened the original event data of three instruments by using *lescreen*, *mescreen* and *hescreen* with the recommended criteria in the user manual¹. The spectra and light curves were extracted by using the tools *lespecgen*, *mespecgen*, *hespecgen*, *lelccgen*, *melccgen* and *helccgen* for the target, and using the tools *lebkmap*, *mebkmap* and *hebkmap* for the background, respectively. All the spectra were grouped with a minimum count of 25 per bin.

The net light curves were calculated with *lcmath*. We then used the *powerspec* in *XRONOS* package to compute the power density spectrum (PDS) in Leahy normalization (Leahy et al. 1983). The net light curves with a time resolution of 1/512 seconds were divided into segments with a length of 512 seconds for producing the PDSs. So the frequency resolution of the PDS is 1/512 Hz and the Nyquist frequency is 256 Hz.

3.2 *NICER* data reduction

The raw data were first reprocessed by using task *nicer12* in the *NICER* software package *NICERDAS*. The source and background spectra, ancillary response files (ARFs) and response matrix files (RMFs) were all extracted by using the pipeline task *nicer13-spect*. During the above procedure, the *SCORPEON* background model was chosen, and the recommended systematic error from the calibration file was applied. The spectra were grouped with a minimum count of 25 per bin.

3.3 X-ray timing analysis

We excluded the soft state from MJD 58310 to 58383 for timing analysis of *Insight*-HXMT data. The PDSs were then logarithmically re-binned with an increment factor of 0.025 in frequency and formatted to be compatible with *XSPEC* (Ingram & Done 2012). We then used a combination of Lorentzian functions and a constant to fit the PDSs in *XSPEC* (v12.12.1): two or four Lorentzians for the BLNs, two or three Lorentzians for the QPO and its harmonic and/or subharmonic and a constant for the white noise. The PDS of the data from LE and ME detectors on the *Insight*-HXMT can be described by a QPO and two BLN components while the data from HE detectors will use two additional Lorentzians to supply the BLN components. Some *NICER* observations during the IMS were used since *Insight*-HXMT observation is absent during the period of MJD 58301–58305 (obsID 1200120192–1200120197). Notably, the QPOs in the observations 1200120196 and 1200120197 exhibited dramatic and rapid changes (Stiele & Kong 2020; Homan et al. 2020). Consequently, we divided the two observations into several segments based on the dynamic power spectra (Homan et al. 2020), in order to study the timing evolution in detail. The *NICER* PDSs consist of one to three BLN components and one or two QPO components. The uncertainties of all the parameters were calculated from the Markov Chain Monte Carlo (MCMC) method by the implementation of *emcee* in *XSPEC*². Using the best-fitting results of PDSs, we calculated the fractional RMS = $\sqrt{K/\langle x \rangle}$, where K is the normalisation of the Lorentzian function and $\langle x \rangle$ is the mean count rate (Leahy et al. 1983; van der Klis 1989).

¹ <http://hxmtcn.ihep.ac.cn/SoftDoc.jhtml>

² https://github.com/zoghbi-a/xspec_emcee

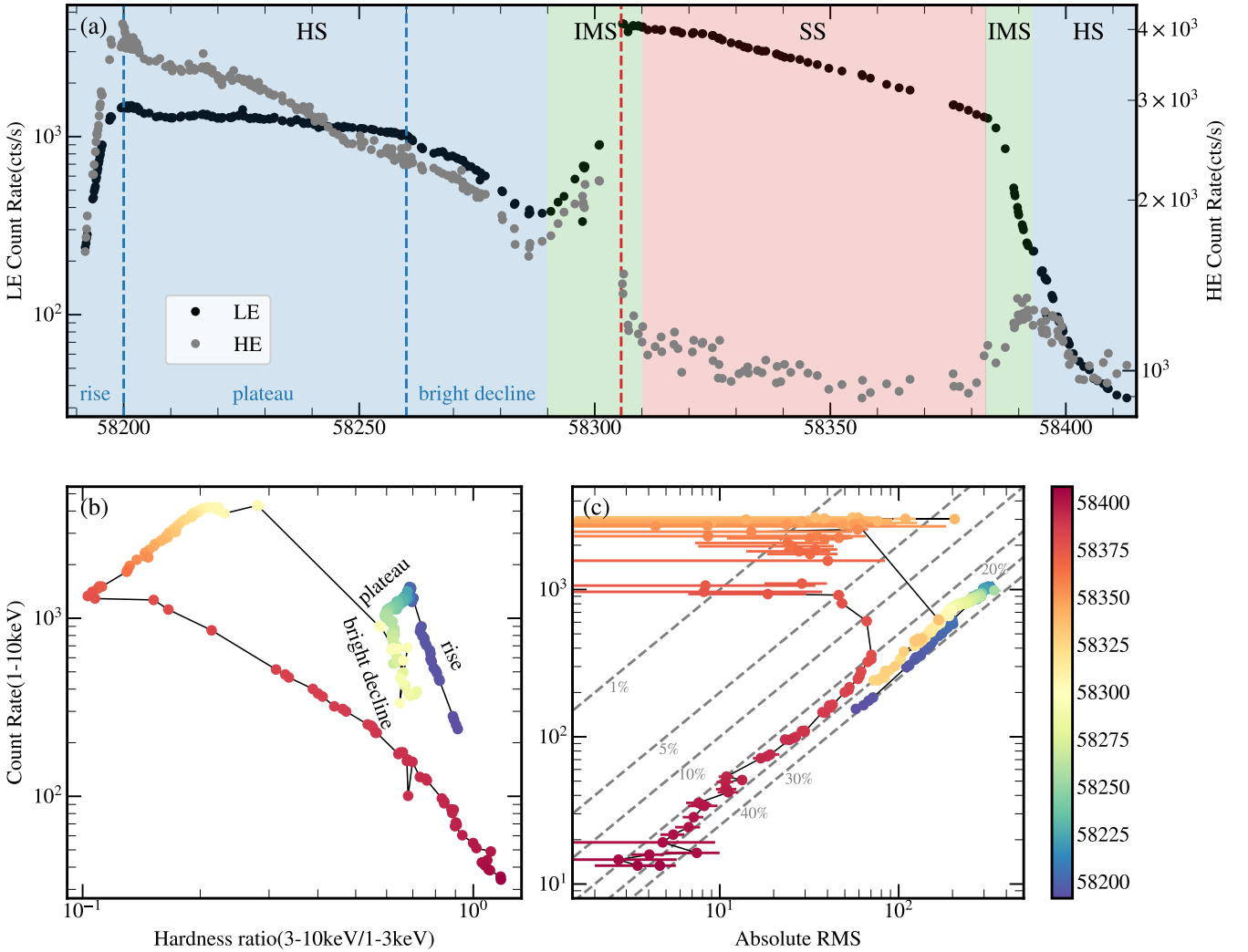


Figure 1. *Insight*-HXMT light curve, hardness-intensity diagram and absolute RMS-intensity diagram of MAXI J1820+070 during the 2018 outburst. (a) Light curves obtained from LE and HE of *Insight*-HXMT. The colors of the background represent the spectral states: blue for the hard state, green for the intermediate state and red for the soft state. The blue dashed lines separate three phases of the rising hard state: the rise, plateau and bright decline phases. The red dashed line represents MJD 58305.60 when the transient jet ejected according to Wood et al. (2021). (b) The *Insight*-HXMT hardness-intensity diagram, defined as the total 1–10 keV count rate vs. the ratio of hard (3–10 keV) to soft (1–3 keV) count rates. The three phases of the rising HS correspond to the three curves of the small “ η ”-like track on the upper right. (c) The absolute RMS-intensity diagram, with the grey lines corresponding to the values of fractional RMS. Both absolute RMS and fractional RMS are determined in the 0.1–64 Hz from *Insight*-HXMT/LE PDS. The color bar on the right corresponds to the observation time.

3.4 X-ray spectral analysis

We performed the spectral fitting through XSPEC v12.12.1 by using the chi statistic. Different models were applied in different spectral states. During the hard and intermediate states of the outburst rise phase, we applied the model $\text{constant} * \text{TBabs} * (\text{diskbb} + \text{relxillCp} + \text{gaussian})$ to fit X-ray spectra in the 2–150 keV. The constant factor was used to coordinate calibration differences between different instruments, where the constant for LE was fixed at 1. The equivalent hydrogen column density (N_H) of TBabs was fixed at $0.15 \times 10^{22} \text{ cm}^{-2}$ (Uttley et al. 2018). The diskbb is a multi-blackbody component, which accounts for the accretion disk radiation. The relxillCp (version 2.3) is a relativistic reflection model that calculates the spectrum from an accretion disk illuminated by the corona (García et al. 2014; Dauser et al. 2022). In our spectral fitting, we fixed the black hole spin at $a = 0.14$ (Zhao

et al. 2021) and the inclination angle at $i = 63^\circ$ (Atri et al. 2020). We tied the normalization N_{disk} of the diskbb to the inner disk radius R_{in} (in unit of R_g) in relxillCp as $816 R_{\text{in}}^2$ (Gao et al. 2023) by ignoring the uncertainties of the distance and inclination angle. On the other hand, the real R_{in} is affected by the color-correction factor, boundary condition and disk wind (e.g. Kubota et al. 1998; Zdziarski et al. 2022). For simplicity, we only used a continuous power-law emissivity and fixed the index at $q_1 = q_2 = 3.0$, and a constant ionization ($\text{iongrad_type} = 0$). The gaussian was used to account for a narrow component near the iron K emission line (~ 6.4 keV). Finally, we used the cflux to get the flux of the diskbb and relxillCp in the 0.1–100 keV energy band, then got the flux of reflection and Comptonization components by setting reflection fraction refl_frac as zero. During and after the soft state, we applied the model $\text{constant} * \text{TBabs} * (\text{diskbb} + \text{nthComp} + \text{gaussian})$ to fit

the broadband X-ray spectrum. Then, we also used `cflux` to calculate the flux of the `diskbb` and `nthComp` in 0.1–100 keV energy band. The uncertainties of all the parameters were calculated using the `emcee` in `XSPEC`.

Because of the absence of *Insight*-HXMT observation around MJD 58301 to 58305 in the IMS, we used the *NICER* data as the supplementary. We also generated the energy spectra for each segment of obsID 1200120196 and 1200120197. Then we applied the same model as used for *Insight*-HXMT data during this period to fit the spectra in the 1–10 keV. For simplicity, we fixed the electron number density $\log N$, iron abundance A_{Fe} and electron temperature kT_e at 10^{20} cm^{-3} , 5.0 and 100.0 keV, respectively.

4 X-RAY SPECTRAL AND TIMING EVOLUTION DURING THE 2018 OUTBURST

4.1 Unique evolution of rising HS

The count rates of MAXI J1820+070 from LE and HE of *Insight*-HXMT are plotted in Figure 1a, and the hardness-intensity diagram (HID) and absolute RMS-intensity diagram (RID) are also shown in Figure 1b and c. The light curve of MAXI J1820+070 shows a multi-peaked outburst profile (Chen et al. 1997). The first peak remains in the hard state, while its HID exhibits a small loop, which looks like a “ η ” track (Figure 1b). The rising HS is divided into three phases: the rise, plateau and bright decline phases (e.g. Stiele & Kong 2020; De Marco et al. 2021), which roughly corresponds to the three curves of the small “ η ”. The rise phase is from the start of the outburst to MJD 58200 when the count rate reaches the peak and then begins to decrease slowly. The plateau phase is from MJD 58200 to 58260, and the bright decline phase is from 58260 to MJD 58290. The absolute RMS and count rate do not follow a single positive correlation (Figure 1c; see also Stiele & Kong 2020). This loop evolution of rising HS in HID/RID has never been shown in other BHXRBs (Belloni 2010; Belloni & Motta 2016). Even in the other outbursts with multiple peaks, their HID/RID usually do not show a loop trend during the rising HS, such as the outbursts in XTE J1550–564, GX339-4 and GRO J1655–40 (e.g. Sobczak et al. 2000; Debnath et al. 2008; Clavel et al. 2016).

During the rising HS, our timing and spectral analysis results show a clear distinction between this special plateau phase with the rise and bright decline phase. Notably, despite the gradual decline of the count rate during the plateau phase, the Comptonization Luminosity L_C calculated from model `relxillCp` remains almost constant (see Figure 3). The reflection fraction R_f is large (> 1) during the plateau phase, which is the largest among BHXRBs at this luminosity level (You et al. 2023b). The QPO frequency $\nu_{\text{C,QPO}}$ exhibits a positive and parallel correlation with the total X-ray luminosity L_X during the rise and the bright decline phases while the correlation is negative in the plateau phase (see Figure 7a).

4.2 X-ray luminosity and spectral parameter evolution

Based on spectral analysis, we present the evolution of the main parameters of the models in Figure 2. The hard and intermediate state are applied with a complex model `constant*TBabs*(diskbb+relxillCp+gaussian)`. The reflection fraction R_f increases in the rise phase of HS and subsequently undergoes a gradual decline until the SS. Please note that the definition of R_f from `relxillCp` with version older than 1.4.1 is different

³. The electron temperature kT_e decreases in the rise phase of HS, increases slowly until the end of hard state, and drops again in the HIMS. During other periods of the outburst, it is not well-constrained. The normalization N_{disk} initially decreases quickly in the rise phase and decreases slowly in the plateau and bright decline phase of the HS. Then it begins to increase during the IMS. The photon index Γ manifests different growth rates between the rise and plateau phases of HS, followed by a decrease during the bright decline phase and a rapid increase during the IMS. The inner disk temperature T_{in} increases rapidly in the rise phase of the HS and increases slowly before the IMS is reached. During the IMS, T_{in} sharply increases and reaches the level of SS.

During and after the SS, we applied the model `constant*TBabs*(diskbb+nthComp+gaussian)` for spectral fitting. Then the T_{in} starts to decrease exponentially until the end of SS accompanied by a relatively constant N_{disk} , which is consistent with the standard thin disk (Shakura & Sunyaev 1973). Due to the hard X-ray tail in the *Insight*-HXMT spectra, Γ at an early stage of SS is lower than that in SIMS (see also Fabian et al. 2020; Mummery et al. 2024). Γ shows fluctuations until we cannot constrain well and fix it at 2.4 for the rest of SS. During the decaying IMS, Γ gradually drops to the HS level. The evolution of the spectral parameters in different spectral states is also reported in You et al. (2021); Peng et al. (2023); Fan et al. (2024).

The X-ray luminosity of different spectral components calculated in the energy range of 0.1–100 keV is presented in Figure 3. In the rise phase of HS, L_X , L_R and L_C all increase. However, L_R reaches peak synchronously with R_f , and L_C reaches its peak earlier. Subsequently, L_R and L_X decrease until the end of HS. Notably, L_C remains relatively constant during the plateau phase and then decreases in the bright decline phase of HS. During the rising IMS, there is a significant increase in luminosities of different spectral components except L_R , particularly around the period of transient jet ejection (Figure 3). Afterward, L_D surpasses L_C . During the SS, L_D exhibits an exponential decline. In the decaying IMS, L_D continues to decrease at a steeper rate, while L_C experiences a small flare (Figure 3).

4.2.1 Relationships between L_X and spectral parameters

The relationship between photon index Γ and total X-ray luminosity L_X is presented in Figure 4a. It is evident that L_X and Γ show almost identical “q”-like evolution with HID even the small “ η ”-like track during the rising HS. When the reflection fraction R_f exceeds 1, the reflection component surpasses the Compton component below the energy of the reflection hump ($\lesssim 30$ keV; Dauser et al. 2014). Consequently, the photon index (also hardness ratio) is primarily influenced by the reflection component rather than the Compton component in X-ray spectra when $R_f > 1$. Notably, the slope of the reflection spectra in the 2–10 keV energy range are always steeper than that of the Compton spectra (Figure A1), resulting in a larger Γ and also hardness. So the Γ (also hardness) is determined by either Compton ($R_f < 1$) or reflection ($R_f > 1$) component depending on the R_f . The positive correlation observed between luminosity and the photon index in the bright hard state of other BHXRBs is primarily driven by Compton emission (e.g. Yang et al. 2015; Yan et al. 2020; You et al. 2023b). As a result, this behavior is not observed during the rising HS with $R_f > 1$ in MAXI J1820+070. So the distinctive

³ <http://www.sternwarte.uni-erlangen.de/~dauser/research/relxill/index.html>

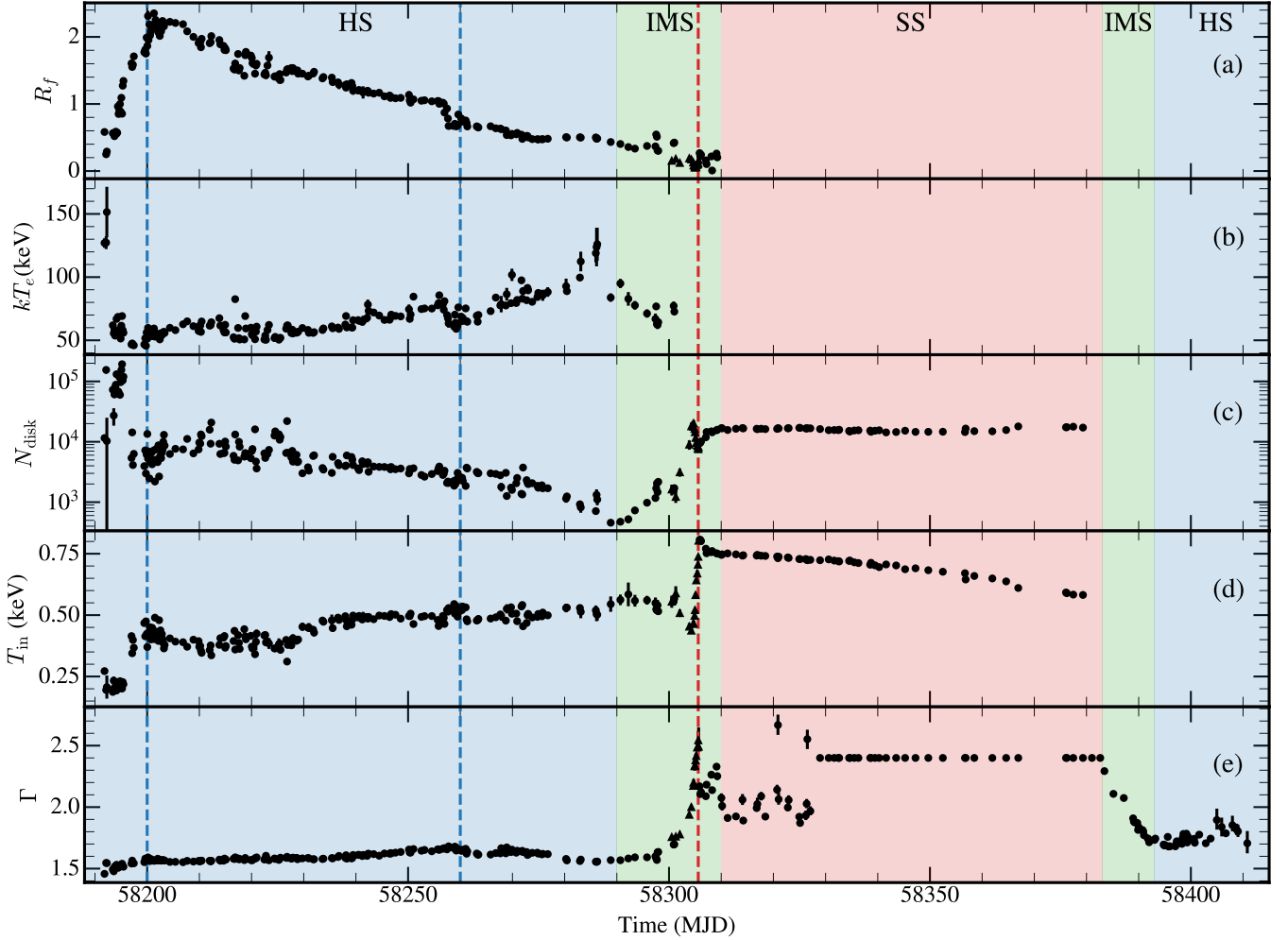


Figure 2. Time evolution of spectral parameters. From top to bottom: the reflection fraction R_f , the electron temperature kT_e , the normalization of the diskbb N_{disk} , the inner disk temperature T_{in} , the photon index Γ . The dots are derived from *Insight*-HXMT data and the triangles are derived from *NICER* data. The colors of the background and dashed lines are the same as in [Figure 1](#).

evolution of R_f leads to the unique “ η ”-like track in L_X - Γ and HID during the rising HS.

The relationship between the L_X and the ratio of L_C to L_D is shown in [Figure 4b](#). At the end of outburst decay, the diskbb is no longer required for the spectral fitting. So the L_C/L_D is calculated by using the last best-fitting L_D . This diagram also presents a “q”-like pattern similar to HID and L_X - Γ . Notably, the parameters Γ and hardness follows an “ η ”-like track during the rising HS, which is not observed in L_C/L_D ([Figure 4](#)). This result also highlights that the Γ during the rising HS is not always determined by the Compton component. Since the Γ exhibits a monotonically negative correlation with the L_C/L_D in the Comptonization scenario (e.g. [Haardt & Maraschi 1991](#); [Beloborodov 1999](#)).

The relationships between total X-ray luminosity L_X and both the reflection fraction R_f and electron temperature kT_e are respectively shown in [Figure 5a](#) and [Figure 5b](#). During the rising HS, a positive correlation is observed between L_X and R_f (see also [You et al. 2023b](#)), which then inverts to a negative correlation in the IMS. Concurrently, kT_e demonstrates a uniform negative correlation with L_X when it can be accurately constrained by our model during both the HS and HIMS (e.g. [Yan et al. 2020](#); [You et al. 2023b](#)).

4.3 Type-C QPO evolution

The evolution of centroid frequency of type-C QPO is present in [Figure 6](#). We could detect the type-C QPO from around MJD 58193.42 until MJD 58305.61 when the source reaches the SIMS. The centroid frequency of QPO $\nu_{C,QPO}$ ranges from 0.01 to 8.05 Hz and the values obtained from the same exposure ID in different detectors (LE, ME and HE) are nearly identical. The $\nu_{C,QPO}$ evolution obtained from *Insight*-HXMT is almost the same as that from *NICER* data ([Stiele & Kong 2020](#)).

The QPO frequency apparently changes at different rates during different phases ([Figure 6](#)). [Buisson et al. \(2018\)](#) has claimed that the QPO frequency exponentially increases with time. We also used exponential function $\nu_{C,QPO} = p_0 e^{(t-t_0)/\tau}$ to fit the $\nu_{C,QPO}$ at different phases. The best-fitting e -folding time scales τ are 7.63 ± 0.78 , 23.99 ± 0.65 , -50.27 ± 7.86 days for the rise, plateau and bright decline phases of HS, respectively ([Figure 6](#)). The $\nu_{C,QPO}$ evolution during the IMS obviously experiences two different increasing rates with e -folding time scales of 8.28 ± 0.76 , and 1.02 ± 0.05 days ([Figure 6](#)).

We also performed timing analysis for the *Insight*-HXMT data during the decaying IMS and HS. But no significant QPO signals

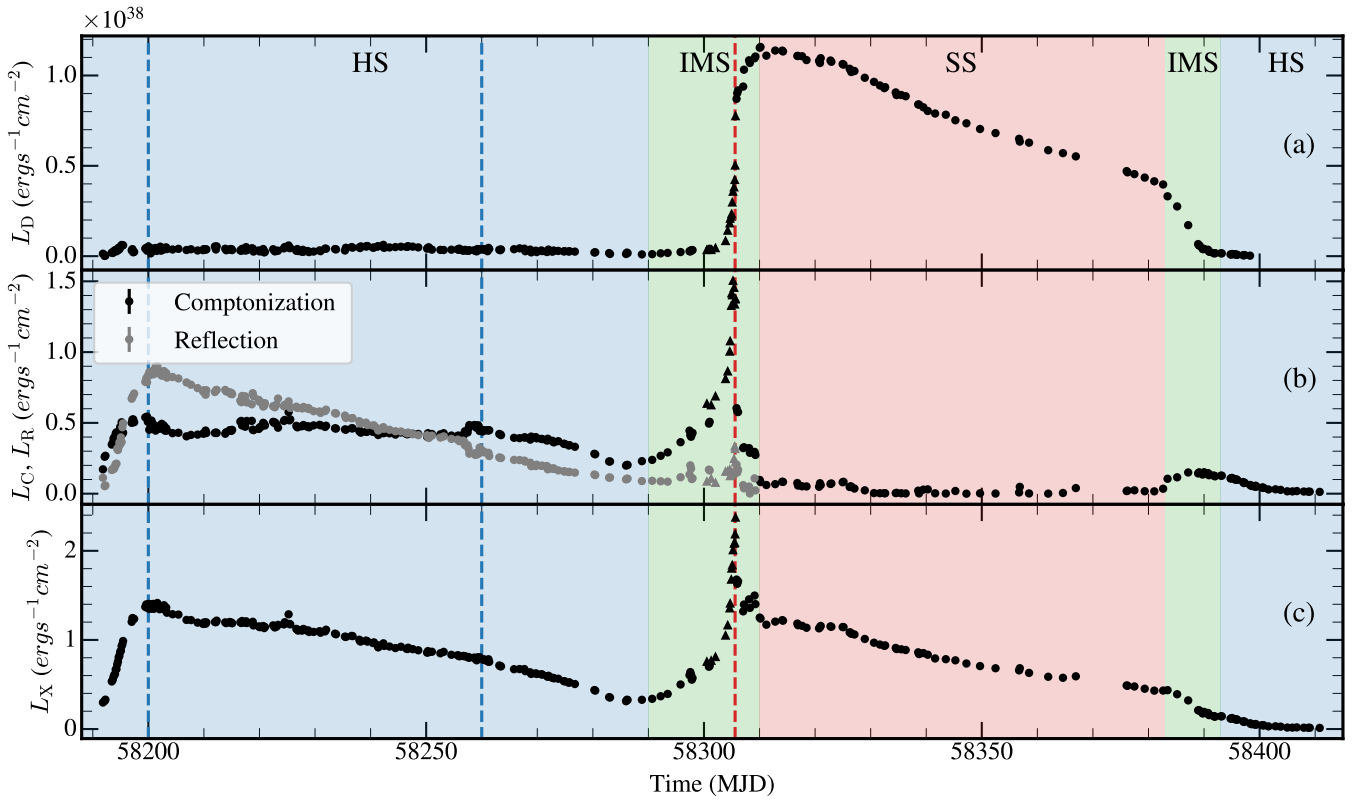


Figure 3. Time evolution of X-ray luminosities in 0.1–100 keV of different spectral components: the disk luminosity (upper panel), the Comptonization luminosity and the reflection luminosity (middle panel) and total luminosity (lower panel). The dots are derived using *Insight*-HXMT data and the triangles are derived using NICER data. The colors of the background and dashed lines are the same as in Figure 1.

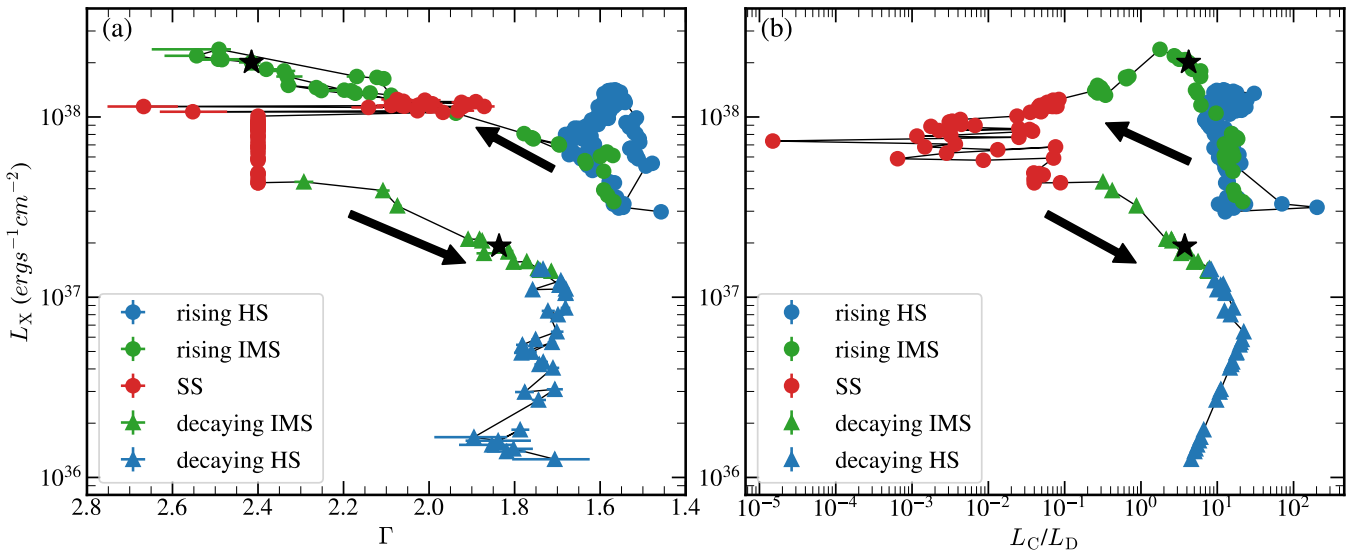


Figure 4. (a) The relationship between photon index Γ and total luminosity L_X during the 2018 outburst. Blue dots, green dots, red dots, green triangles and blue triangles respectively indicate rising hard state and intermediate state, soft state, decaying hard state and intermediate state. The black stars mark the transition luminosities in the outburst rise and decay phases. Arrows indicate the direction of evolution. (b) The relationship between the ratio of Comptonization luminosity L_C to disk luminosity L_D and total luminosity L_X during the 2018 outburst. Symbols and colors are the same as in panel (a).

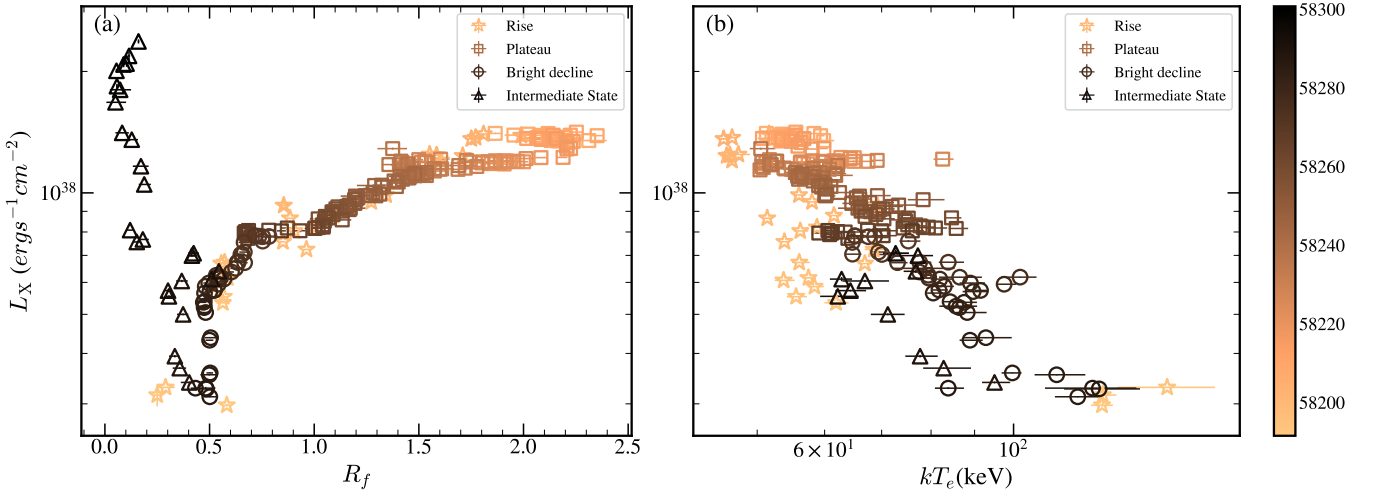


Figure 5. (a) The relationship between the reflection fraction R_f and total luminosity L_X during the hard/hard-intermediate state. The stars, squares, dots and triangles respectively indicate the rise, plateau and bright decline phases in the hard state and intermediate state. (b) The relationship between the electron temperature kT_e and total luminosity L_X during the hard/hard-intermediate state. Symbols and colors are the same as in panel (a). The color bar on the right corresponds to the observation time.

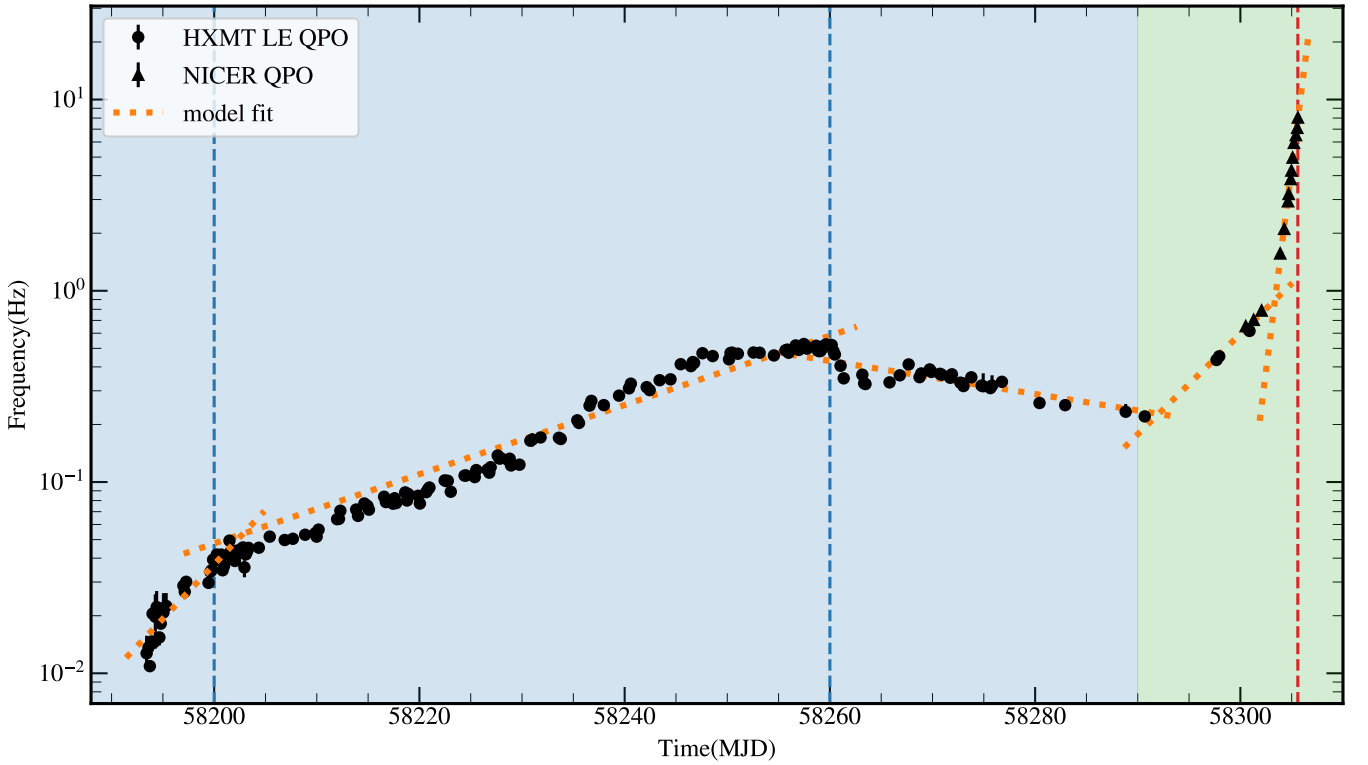


Figure 6. Time evolution of the characteristic frequencies of the type-C QPO. The dots are obtained from *Insight*-HXMT LE data and triangles are from *NICER* data. The orange dotted lines represent the best-fitting exponential functions applied to the data of different phases: the rise, plateau, and bright decline phases in hard state, and two segments separated on MJD 58303 during intermediate state. The colors of the background and dashed lines are the same as in Figure 1.

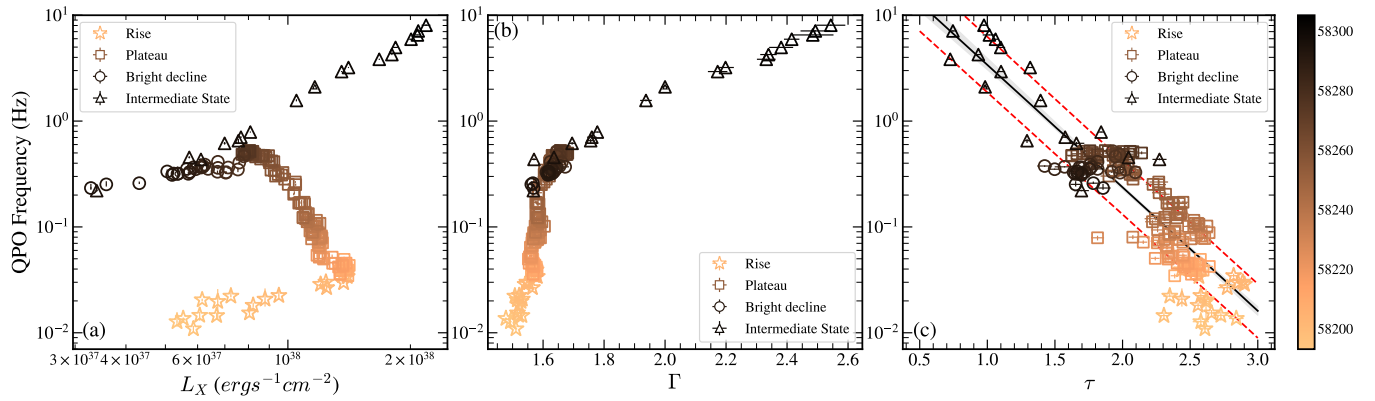


Figure 7. (a) The relationship between type-C QPO frequency and total luminosity L_X . (b) The relationship between type-C QPO frequency and photon index Γ . (c) The relationship between type-C QPO frequency and optical depth τ . The black line indicates the best-fitting linear function. The gray shaded area represents the error region for the slope and offset. The red dashed lines indicate the scattering range of the data. Symbols and colors are the same as in Figure 5. The color bar on the right corresponds to the observation time.

were detected. We noticed that there are some QPO detections with *NICER* data reported in Stiele & Kong (2020). However, only six QPO signals are considered to be significant ($> 3\sigma$). Their frequency and fractional RMS vary chaotically. Consequently, it is difficult to conclusively determine the type and evolution of the detected QPOs during the decaying IMS and HS.

We then investigated the relationships between type-C QPO frequency $\nu_{C,QPO}$ and spectral parameters during the rising HS and HIMS (Figure 7). The $\nu_{C,QPO}$ exhibits a complex correlation with the total X-ray luminosity L_X . Two positive correlations parallelly exist in the rise and bright decline phases of HS and IMS. However, a negative correlation is observed in the plateau phase of HS (Figure 7a). The $\nu_{C,QPO}$ and photon index Γ exhibit an overall positive correlation in the HS and HIMS, with varying slopes across different phases (Figure 7b). It appears that the slopes during the rise, plateau, and bright decline phases of HS and HIMS differ. We also calculated the optical depth τ of Compton component from kT_e and Γ according to the equation in (Zdziarski et al. 1996). As present in Figure 7c, the $\nu_{C,QPO}$ and τ follow a single negative correlation. The best-fitting slope of this correlation is obtained as -1.18 ± 0.04 using the Bayesian method in Buchner (2021). However, the correlation displays a large scatter, with a value of 0.26 ± 0.01 .

4.4 Dramatic changes around the transient jet ejection

We are already aware that significant X-ray spectral and timing changes in the transition between HIMS and SIMS (see Figure 2, Figure 3 and Figure 6), coinciding with two transient jet ejections and a radio flare around MJD 58306 (Bright et al. 2020; Homan et al. 2020; Wood et al. 2021). Approximately 4 hours subsequent to the first ejection, a radio flare is observed. The peak of the radio flare coincides with the second ejection (see Figure 8 and Wood et al. 2021). It is currently uncertain which ejection the radio flare corresponds to. Both ejection times are the best-constrained among BHXRBS (Carotenuto et al. 2024). Due to the extensive coverage of *NICER* observation, we are able to investigate the spectral and timing variation before and after the ejection.

We divided the two observations around jet ejection into 11 segments. The parameters of QPOs detected in each segment are listed in Table A. Notably, the type-C QPO is present in every segment except the last one, which occurs just after the first ejection on MJD 58305.60

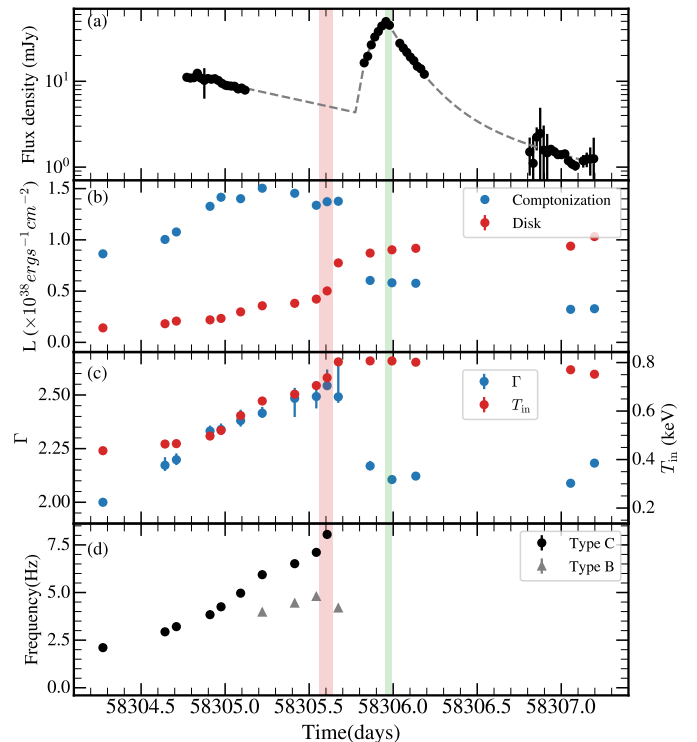


Figure 8. (a) AMI-LA radio light curve (15.5 GHz) from Bright et al. (2020) around the transient jet ejection. The grey dashed line indicates the best-fitting model from Homan et al. (2020): an exponential function for the baseline decay, an additional linear function for the radio flare rise, and an additional power-law function for the radio flare decay phase. (b) The concurrent evolution of the X-ray disk luminosity L_D and the Comptonization luminosity L_C (0.1–100 keV). (c) The concurrent evolution of photon index Γ and inner disk temperature T_{in} . (d) The concurrent evolution of the centroid frequency of type-C and type-B QPOs. The red and green shadows mark the ejection times of two ejected components on MJD 58305.60 ± 0.04 and 58305.97 ± 0.02 , respectively (Wood et al. 2021).

± 0.04 . Additionally, a type-B QPO around 4 Hz emerges roughly 0.4 days before this ejection. It is first detected on MJD 58305.22 and persists for approximately 14 hours. Although the type-B QPOs are not prominently visible in the dynamic PDSs prior to the ejection (see Homan et al. 2020), they are significantly detected in the averaged PDS of certain segments (Table A).

In Figure 8, we also present spectral parameters and X-ray luminosity. Prior to the first ejection, the spectral parameters, specifically the disk temperature T_{in} and photon index Γ , exhibit a sharp increase. After the first ejection, the T_{in} and L_{D} reach the SS level, the Γ and L_{C} show a decrease.

5 DISCUSSION

5.1 The “q”-like HID and the evolution of $L_{\text{X}}-\Gamma$

Similar evolution tracks are anticipated in both the $L_{\text{X}}-\Gamma$ and HID, as the calculated hardness (3–10keV/1–3keV) depends on the slope of the X-ray spectrum, also known as the photon index. Figure 4a displays a “q”-like track between L_{X} and Γ when all data from the entire outburst are included, and a small “ η ”-like track during the rising HS, which is similar to HID (Figure 1). We have also gathered data from several outbursts with comprehensive observations that span the full duration of the outburst from the literature (Sobczak et al. 2000; Debnath et al. 2008; McClintock et al. 2009). We found that L_{X} and Γ follow a roughly “q”-like track in all three outbursts similar to the HID (see Figure A2). The data in the hard state (right part of the “q”) roughly follows a “v”-like correlation, aligning with previous work. The significant scatter of the right branch of “v”-like correlation (e.g. Fig.2 in Yan et al. 2020) is evidently due to the different bend points at the upper right of the “q” track in different outbursts, i.e., the luminosity where the HS can reach.

In the case of thermal Comptonization, the photon index Γ monotonically decreases with $L_{\text{corona}}/L_{\text{seed}}$ (e.g. Haardt & Maraschi 1991; Beloborodov 1999). In this work, the L_{corona} and L_{seed} can be represented by the Compton and disk luminosity, respectively. The L_{X} and $L_{\text{C}}/L_{\text{D}}$ indeed follows a similar “q” track to L_{X} and Γ (see Figure 4b and also Dunn et al. 2010). So the evolution of the corona, which is responsible for the Comptonization, determines the “q”-like tracks (Figure 1b and Figure 4).

The H-S transition luminosity during the outburst rise is usually several times larger than the S-H transition luminosity during the outburst decay (e.g. Yu & Yan 2009; Tetarenko et al. 2016), even the hardness ratio or photon index is similar. This phenomenon is called hysteresis effect, which is universal in outbursts experiencing state transitions (e.g. Maccarone 2003). According to the definition in Yu & Yan (2009), the transition luminosities of H-S and S-H correspond to hard X-ray peaks before and after the SS. For MAXI J1820+070, the H-S transition luminosity is $1.8 \times 10^{38} \text{ erg s}^{-1}$, which is almost one order of magnitude higher than the S-H transition luminosity ($1.9 \times 10^{37} \text{ erg s}^{-1}$, see also Figure 4). The Compton luminosity of H-S transition is also roughly ten times higher than that of S-H transition (1.4×10^{38} and $1.5 \times 10^{37} \text{ erg s}^{-1}$). So the discrepancy of the transition luminosity is dominated by the Compton component.

Non-stationary accretion flow has been proposed to drive the H-S transition luminosity during outburst rise, i.e. the transition luminosity is higher when the mass accretion rate increases faster (Yu et al. 2004; Yu & Yan 2009). During the outburst decay, the S-H transition luminosity remains in a very narrow range (e.g. Maccarone 2003; Vahdat Motlagh et al. 2019), since S-H transition occurs from a stationary standard accretion disk (Yu & Yan 2009). For MAXI

J1820+070, the rapid increase of the hard X-ray flux before transition and the corresponding H-S transition luminosity (Figure 3 and Figure 4) is consistent with the above scenario. So the hysteresis effect is mainly driven by the non-stationary accretion flow during the outburst rise, which produces the Compton emission dominated the hard X-ray.

Hot accretion flow is the predominant model to produce the Compton component (see reviews by Yuan & Narayan 2014; Liu & Qiao 2022). In such a framework, the hot accretion flows can only exist below the critical luminosity $L < \alpha^2 L_{\text{Edd}}$ (e.g. Esin et al. 1997; Xie & Yuan 2012), where the α is the viscosity parameter of hot accretion flow and the L_{Edd} is the Eddington luminosity. So an increasing α can maintain the hot accretion flow at high luminosity regime, to make the H-S transition luminosity higher (Begelman & Armitage 2014; Cao 2016; Li & Qiao 2023). As a result, the increasing α may play a similar role as the proposed non-stationary accretion flow in Yu & Yan (2009). The enhancement of the magnetic field and/or outflow is able to increase α (Bai & Stone 2013; Cao 2016).

Jet or its base is also an alternative origin of the Compton emission. Some X-ray spectral and timing properties during the state transition can be well explained by jet-like corona (see the discussions in subsequent sections). Marcel et al. (2019) has fine-tuned two independent parameters r_{J} and \dot{m}_{in} of the jet-accretion disk model to replicate the “q”-like evolutionary track, where r_{J} is the transition radius between jet and accretion disk, \dot{m}_{in} is the mass accretion at the inner disk radius. This model is quite similar to the truncated disk model (Esin et al. 1997; Done et al. 2007). However, it is still unknown what mechanism drives the evolution of r_{J} .

5.2 Inner radius of accretion disk/reflected component

We used the multiple blackbody model `diskbb` to fit the thermal component in HS, IMS and SS. The square root of the normalization of this model $\sqrt{N_{\text{disk}}}$ can be used as the proxy of the inner radius of the accretion disk (Kubota et al. 1998). The nearly constant N_{disk} and exponential decreasing of T_{in} during the SS (Figure 2) are consistent with standard accretion disk that the inner radius reaches the innermost stable circular orbit R_{ISCO} (Shakura & Sunyaev 1973).

In the spectral fitting of the rising HS and IMS, we employed the relativistic reflection model `relxillCp` and linked the inner radius of the reflected component to the N_{disk} . During the HS, the N_{disk} continuously decreases (Figure 2), coinciding with a decrease in the reverberation time lag between the corona and the reflected component. This behavior agrees with the expected reflection from a truncated accretion disk or a contracting corona (Kara et al. 2019; De Marco et al. 2021). However, the N_{disk} increases after entering the IMS (Figure 2), which is also consistent with the evolution of the reverberation time lag (De Marco et al. 2021; Wang et al. 2021). Wang et al. (2021) proposed that a jet-like corona vertically contracts/expands resulting in the observed evolution of the reverberation time lag before and after the state transition (see also Kylafis et al. 2008; You et al. 2021; Cao et al. 2022; Méndez et al. 2022; Wang et al. 2022b).

However, the best-fitting N_{disk} during the IMS are obviously smaller than those during the SS (Figure 2, see also Motta et al. 2009), which indicates that the reflected component may not be an accretion disk if the constant N_{disk} in the SS represents the R_{ISCO} . In such a case, the N_{disk} may be the proxy of the area of the reflected component. During the HS, the corona contracts, resulting in a natural decrease in time lag and a reduction in the irradiated area. Conversely, during the IMS, the corona expands, leading to an increase in both the time lag and irradiated area. The spectral fitting by

Buisson et al. (2019) also reveals that the height of the upper corona varies in a similar manner when the two lampposts geometry is applied. On the other hand, the unusual decreasing of reflection fraction R_f after the rise phase of HS (Figure 2) also can be explained by the jet-like corona (You et al. 2021). So the spectral evolution during the HS and IMS is consistent with a contracting/expanding jet-like corona.

However, the nature of reflected component during the plateau and bright decline of HS remains puzzling, if its size is smaller than the R_{ISCO} of the accretion disk. The cold cloud embedded in the hot plasma is a possible candidate (e.g. Krolik 1998; Wang et al. 2012). In such a geometry, the reflection fraction is expected to be large. So the unusually large R_f and the additional narrow iron line also support this conjecture (see e.g. Malzac & Celotti 2002; Merloni et al. 2006; Yu et al. 2018).

5.3 Type-C QPO frequency, corona geometry and Comptonization

The type-C QPO is a predominant characteristic detected in the HS and HIMS, the oscillated photons of which are generally believed to originate from the component producing the Compton emission (e.g. Lee & Miller 1998; Psaltis & Norman 2000; Bellavita et al. 2022; Ma et al. 2021; Gao et al. 2023). So it is important to investigate the QPO properties and the spectral parameters of Compton component. The correlation between the QPO frequency $\nu_{\text{C,QPO}}$ and the photon index Γ of the Compton component has been widely studied (e.g. Vignarca et al. 2003; Shaposhnikov & Titarchuk 2009; Stiele et al. 2013; Wang et al. 2022a). The $\nu_{\text{C,QPO}}$ usually positively correlates with the Γ over two orders of magnitude frequency range, and the Γ becomes saturated above a certain frequency in few sources (e.g. Vignarca et al. 2003; Shaposhnikov & Titarchuk 2009). It is generally believed that the mass accretion rate drives the evolution of both X-ray spectral and timing properties of BHXRB (see reviews in Done et al. 2007; Gilfanov 2010). The Γ and the $\nu_{\text{C,QPO}}$ both increase with X-ray luminosity, resulting in a positive correlation (e.g. Revnivtsev et al. 2001; Mereminskiy et al. 2019; Wang et al. 2022a). However, $\nu_{\text{C,QPO}}$ in MAXI J1820+070 displays a complex correlation with L_X (Figure 7a), and Γ exhibits a “ η ”-like track along L_X (Figure 4). These results suggest that the mass accretion rate is not the only factor influencing the evolution of the spectral and timing properties of the corona.

MAXI J1820+070 also shows a positive correlation between $\nu_{\text{C,QPO}}$ and Γ with varying slopes across different phases of HS and HIMS (Figure 7b). The $\nu_{\text{C,QPO}}$ and τ exhibit a consistent negative correlation across various phases of HS and HIMS (Figure 7c). These correlations provide compelling evidence that the Comptonization is the driving force behind the evolution of the QPO frequency. Recently, some models have been proposed to explain the properties of the type-C QPO based on the Comptonization process (e.g. Bellavita et al. 2022; Mastichiadis et al. 2022). Specifically, the interplay between thermal and Compton components, which influences optical depth and electron temperature during Comptonization, can produce an oscillation roughly consistent with type-C QPO (Mastichiadis et al. 2022).

In some other models, the QPO frequency is usually thought to inversely correlate to the characteristic scale of the corona and/or the inner radius of the accretion disk (e.g. Ingram et al. 2009; Cabanac et al. 2010; Marcel et al. 2020; Rawat et al. 2023; Motta & Belloni 2024). So the increasing of QPO frequency during the rise and plateau phases of HS (Figure 6) can be accounted for the shrinking of the inner radius of a truncated accretion disk (De Marco et al. 2021;

Zdziarski et al. 2021) or a contracting corona (Kara et al. 2019; Wang et al. 2021, 2022b). However, the observed decreasing in QPO frequency during the bright decline, and its subsequent increasing during the IMS (Figure 6), is challenging to be explained by the behavior of a contracting and then expanding jet-like corona inferred from the reverberation lag and X-ray spectral evolution (Wang et al. 2022b).

The QPO frequency may alternatively be proportional to a characteristic timescale for ejecting mass as a damped oscillator in a jet-like corona model. As a result, the $\nu_{\text{C,QPO}} \propto R_0^2 n_{e,0}$ (Kylafis et al. 2008), where the R_0 is the jet base, and $n_{e,0}$ is the electron number density of the jet base. The expanding jet-like corona during the IMS naturally causes the rapid increase of the QPO frequency. The optical depth in such corona should also be a function of R_0 and $n_{e,0}$. However, the specific relation between τ and Γ in the jet-like corona should be investigated in order to quantitatively understand the correlations between $\nu_{\text{C,QPO}}$ and τ/Γ .

5.4 The association between rapid transition and radio ejection

It is widely recognized that transient jet ejections are associated with X-ray spectral state transitions (Fender et al. 2004), wherein Compton-dominated spectra shift to thermally dominated spectra. The well-sampled observations of MAXI J1820+070 offer a unique opportunity to investigate the temporal connection between ejection events and spectral state transitions. Remarkably, the last occurrence of type-C QPO coincided precisely with the first ejection within one hour. Subsequent to this ejection, the Compton luminosity sharply decreased more than two times within 0.19 days. So the observations of MAXI J1820+070 establish a temporal connection between the corona and ejection within timescale of hours (see also Homan et al. 2020), which the corona is responsible for the Compton emission and the type-C QPO. One plausible scenario is that the corona or part of the corona is ejected, subsequently allowing the disk component to dominate the X-ray spectrum. The dominance of ions in the ejection composition further supports this hypothesis (Zdziarski & Heinz 2024). Additionally, the corona transforming into an ejected jet has been proposed in the microquasar GRS 1915+105 (Mirabel et al. 1998; Méndez et al. 2022). A similar scenario has been proposed for the active galactic nuclei (AGNs) harboring super-massive BH, such as 3C 120 (Marscher et al. 2002) and 3C 111 (Chatterjee et al. 2011), in which the observed X-ray dips are associated with the radio ejections.

ACKNOWLEDGEMENTS

We would like to thank the helpful discussion with Bei You, Fuguo Xie and Phil Uttley. This work made use of the data from Insight-HXMT mission, a project funded by China National Space Administration (CNSA) and the Chinese Academy of Sciences (CAS). This work was supported in part by the Natural Science Foundation of China (grants U1838203, U1938114, 12373049, 12361131579 and 12373050).

DATA AVAILABILITY

The *Insight-HXMT* and *NICER* data underlying this article are available in the public archive <http://archive.hxmt.cn/proposal> and <https://heasarc.gsfc.nasa.gov/docs/archive.html>.

REFERENCES

- Atri P., et al., 2020, *MNRAS*, **493**, L81
- Baglio M. C., Russell D. M., Lewis F., 2018, *The Astronomer's Telegram*, **11418**, 1
- Bai X.-N., Stone J. M., 2013, *ApJ*, **767**, 30
- Begelman M. C., Armitage P. J., 2014, *ApJ*, **782**, L18
- Bellavita C., García F., Méndez M., Karpouzas K., 2022, *MNRAS*, **515**, 2099
- Belloni T. M., 2010, in Belloni T., ed., , Vol. 794, *Lecture Notes in Physics*, Berlin Springer Verlag. Springer-Verlag Berlin Heidelberg, p. 53, doi:10.1007/978-3-540-76937-8_3
- Belloni T. M., Motta S. E., 2016, in Bambi C., ed., *Astrophysics and Space Science Library* Vol. 440, *Astrophysics of Black Holes: From Fundamental Aspects to Latest Developments*. p. 61 (arXiv:1603.07872), doi:10.1007/978-3-662-52859-4_2
- Belloni T., Psaltis D., van der Klis M., 2002, *ApJ*, **572**, 392
- Beloborodov A. M., 1999, *ApJ*, **510**, L123
- Bright J., Fender R., Motta S., 2018, *The Astronomer's Telegram*, **11420**, 1
- Bright J. S., et al., 2020, *Nature Astronomy*, **4**, 697
- Bucher J., 2021, *The Journal of Open Source Software*, **6**, 3001
- Buisson D., Fabian A., Alston W., Walton D., Kara E., Garcia J., Homan J., Tomsick J., 2018, *The Astronomer's Telegram*, **11578**, 1
- Buisson D. J. K., et al., 2019, *MNRAS*, **490**, 1350
- Cabanac C., Henri G., Petrucci P. O., Malzac J., Ferreira J., Belloni T. M., 2010, *MNRAS*, **404**, 738
- Cao X., 2016, *ApJ*, **817**, 71
- Cao X., et al., 2020, *Science China Physics, Mechanics, and Astronomy*, **63**, 249504
- Cao Z., Lucchini M., Markoff S., Connors R. M. T., Grinberg V., 2022, *MNRAS*, **509**, 2517
- Carotenuto F., Fender R., Tetarenko A. J., Corbel S., Zdziarski A. A., Shaik G., Cooper A. J., Di Palma I., 2024, *arXiv e-prints*, p. arXiv:2405.16624
- Casella P., Belloni T., Homan J., Stella L., 2004, *A&A*, **426**, 587
- Chatterjee R., et al., 2011, *ApJ*, **734**, 43
- Chen W., Shrader C. R., Livio M., 1997, *ApJ*, **491**, 312
- Chen Y., et al., 2020, *Science China Physics, Mechanics, and Astronomy*, **63**, 249505
- Clavel M., Rodriguez J., Corbel S., Coriat M., 2016, *Astronomische Nachrichten*, **337**, 435
- Corral-Santana J. M., Casares J., Muñoz-Darias T., Bauer F. E., Martínez-Pais I. G., Russell D. M., 2016, *A&A*, **587**, A61
- Dauser T., Garcia J., Parker M. L., Fabian A. C., Wilms J., 2014, *MNRAS*, **444**, L100
- Dauser T., García J. A., Joyce A., Lickleder S., Connors R. M. T., Ingram A., Reynolds C. S., Wilms J., 2022, *MNRAS*, **514**, 3965
- De Marco B., Zdziarski A. A., Ponti G., Migliori G., Belloni T. M., Segovia Otero A., Dzielak M. A., Lai E. V., 2021, *A&A*, **654**, A14
- Debnath D., Chakrabarti S. K., Nandi A., Mandal S., 2008, *Bulletin of the Astronomical Society of India*, **36**, 151
- Denisenko D., 2018, *The Astronomer's Telegram*, **11400**, 1
- Done C., Gierliński M., Kubota A., 2007, *A&ARv*, **15**, 1
- Dunn R. J. H., Fender R. P., Körding E. G., Belloni T., Cabanac C., 2010, *MNRAS*, **403**, 61
- Esin A. A., McClintock J. E., Narayan R., 1997, *ApJ*, **489**, 865
- Fabian A. C., et al., 2020, *MNRAS*, **493**, 5389
- Fan N., et al., 2024, *arXiv e-prints*, p. arXiv:2404.12161
- Fender R. P., Belloni T. M., Gallo E., 2004, *MNRAS*, **355**, 1105
- Gao C., Yan Z., Yu W., 2023, *MNRAS*, **520**, 5544
- García J., et al., 2014, *ApJ*, **782**, 76
- Gilfanov M., 2010, in Belloni T., ed., , Vol. 794, *Lecture Notes in Physics*, Berlin Springer Verlag. p. 17, doi:10.1007/978-3-540-76937-8_2
- Haardt F., Maraschi L., 1991, *ApJ*, **380**, L51
- Homan J., et al., 2020, *ApJ*, **891**, L29
- Ingram A., Done C., 2012, *MNRAS*, **419**, 2369
- Ingram A., Done C., Fragile P. C., 2009, *MNRAS*, **397**, L101
- Kara E., et al., 2019, *Nature*, **565**, 198
- Kawamuro T., et al., 2018, *The Astronomer's Telegram*, **11399**, 1
- Krolik J. H., 1998, *ApJ*, **498**, L13
- Kubota A., Tanaka Y., Makishima K., Ueda Y., Dotani T., Inoue H., Yamaoka K., 1998, *PASJ*, **50**, 667
- Kylafis N. D., Papadakis I. E., Reig P., Giannios D., Pooley G. G., 2008, *A&A*, **489**, 481
- Leahy D. A., Darbro W., Elsner R. F., Weisskopf M. C., Sutherland P. G., Kahn S., Grindlay J. E., 1983, *ApJ*, **266**, 160
- Lee H. C., Miller G. S., 1998, *MNRAS*, **299**, 479
- Li J., Qiao E., 2023, *MNRAS*, **521**, 3237
- Liu B. F., Qiao E., 2022, *iScience*, **25**, 103544
- Liu C., et al., 2020, *Science China Physics, Mechanics, and Astronomy*, **63**, 249503
- Ma X., et al., 2021, *Nature Astronomy*, **5**, 94
- Maccarone T. J., 2003, *A&A*, **409**, 697
- Malzac J., Celotti A., 2002, *MNRAS*, **335**, 23
- Marcel G., et al., 2019, *A&A*, **626**, A115
- Marcel G., et al., 2020, *A&A*, **640**, A18
- Marscher A. P., Jorstad S. G., Gómez J.-L., Aller M. F., Teräsanta H., Lister M. L., Stirling A. M., 2002, *Nature*, **417**, 625
- Mastichiadis A., Petropoulou M., Kylafis N. D., 2022, *A&A*, **662**, A118
- McClintock J. E., Remillard R. A., Rupen M. P., Torres M. A. P., Steeghs D., Levine A. M., Orosz J. A., 2009, *ApJ*, **698**, 1398
- Méndez M., Karpouzas K., García F., Zhang L., Zhang Y., Belloni T. M., Altamirano D., 2022, *Nature Astronomy*, **6**, 577
- Mereminskiy I. A., Semena A. N., Bykov S. D., Filipova E. V., Lutovinov A. A., Poutanen J., 2019, *MNRAS*, **482**, 1392
- Merloni A., Malzac J., Fabian A. C., Ross R. R., 2006, *MNRAS*, **370**, 1699
- Mirabel I. F., Dhawan V., Chaty S., Rodriguez L. F., Martí J., Robinson C. R., Swank J., Geballe T., 1998, *A&A*, **330**, L9
- Motta S. E., Belloni T. M., 2024, *A&A*, **684**, A209
- Motta S., Belloni T., Homan J., 2009, *MNRAS*, **400**, 1603
- Motta S., Homan J., Muñoz-Darias T., Casella P., Belloni T. M., Hiemstra B., Méndez M., 2012, *MNRAS*, **427**, 595
- Mummery A., Ingram A., Davis S., Fabian A., 2024, *MNRAS*, **531**, 366
- Novikov I. D., Thorne K. S., 1973, in *Black Holes (Les Astres Occlus)*. pp 343–450
- Peng J. Q., et al., 2023, *MNRAS*, **518**, 2521
- Psaltis D., Norman C., 2000, *arXiv e-prints*, pp astro-ph/0001391
- Rawat D., Husain N., Misra R., 2023, *MNRAS*, **524**, 5869
- Remillard R. A., McClintock J. E., 2006, *ARA&A*, **44**, 49
- Revnivtsev M., Gilfanov M., Churazov E., 2001, *A&A*, **380**, 520
- Sakamoto T., et al., 2016, *PASJ*, **68**, S2
- Shakura N. I., Sunyaev R. A., 1973, *A&A*, **24**, 337
- Shaposhnikov N., Titarchuk L., 2009, *ApJ*, **699**, 453
- Shappee B. J., et al., 2014, *ApJ*, **788**, 48
- Shidatsu M., Nakahira S., Murata K. L., Adachi R., Kawai N., Ueda Y., Negoro H., 2019, *ApJ*, **874**, 183
- Subczak G. J., McClintock J. E., Remillard R. A., Cui W., Levine A. M., Morgan E. H., Orosz J. A., Bailyn C. D., 2000, *ApJ*, **544**, 993
- Stiele H., Kong A. K. H., 2020, *ApJ*, **889**, 142
- Stiele H., Belloni T. M., Kalemci E., Motta S., 2013, *MNRAS*, **429**, 2655
- Sunyaev R. A., Truemper J., 1979, *Nature*, **279**, 506
- Tetarenko B. E., Sivakoff G. R., Heinke C. O., Gladstone J. C., 2016, *ApJS*, **222**, 15
- Torres M. A. P., Casares J., Jiménez-Ibarra F., Álvarez-Hernández A., Muñoz-Darias T., Armas Padilla M., Jonker P. G., Heida M., 2020, *ApJ*, **893**, L37
- Tucker M. A., et al., 2018, *ApJ*, **867**, L9
- Uttley P., et al., 2018, *The Astronomer's Telegram*, **11423**, 1
- Vahdat Motlagh A., Kalemci E., Maccarone T. J., 2019, *MNRAS*, **485**, 2744
- Vignarca F., Migliari S., Belloni T., Psaltis D., van der Klis M., 2003, *A&A*, **397**, 729
- Wang J.-M., Cheng C., Li Y.-R., 2012, *ApJ*, **748**, 147
- Wang Y., et al., 2020, *ApJ*, **896**, 33
- Wang J., et al., 2021, *ApJ*, **910**, L3
- Wang P. J., et al., 2022a, *MNRAS*, **512**, 4541
- Wang J., et al., 2022b, *ApJ*, **930**, 18
- Wood C. M., et al., 2021, *MNRAS*, **505**, 3393
- Xie F.-G., Yuan F., 2012, *MNRAS*, **427**, 1580

- Yan Z., Yu W., 2015, *ApJ*, **805**, 87
- Yan Z., Xie F.-G., Zhang W., 2020, *ApJ*, **889**, L18
- Yang Q.-X., Xie F.-G., Yuan F., Zdziarski A. A., Gierliński M., Ho L. C., Yu Z., 2015, *MNRAS*, **447**, 1692
- You B., et al., 2021, *Nature Communications*, **12**, 1025
- You B., et al., 2023a, *Science*, **381**, 961
- You B., Dong Y., Yan Z., Liu Z., Tuo Y., Yao Y., Cao X., 2023b, *ApJ*, **945**, 65
- Yu W., Yan Z., 2009, *ApJ*, **701**, 1940
- Yu W., van der Klis M., Fender R., 2004, *ApJ*, **611**, L121
- Yu X.-D., Ma R.-Y., Li Y.-P., Zhang H., Fang T.-T., 2018, *MNRAS*, **476**, 2045
- Yuan F., Narayan R., 2014, *ARA&A*, **52**, 529
- Zdziarski A. A., Heinz S., 2024, *ApJ*, **967**, L7
- Zdziarski A. A., Johnson W. N., Magdziarz P., 1996, *MNRAS*, **283**, 193
- Zdziarski A. A., Dzielak M. A., De Marco B., Szanecki M., Niedźwiecki A., 2021, *ApJ*, **909**, L9
- Zdziarski A. A., You B., Szanecki M., 2022, *ApJ*, **939**, L2
- Zhang S.-N., et al., 2020, *Science China Physics, Mechanics, and Astronomy*, **63**, 249502
- Zhao X., et al., 2021, *ApJ*, **916**, 108
- van der Klis M., 1989, in Ögelman H., van den Heuvel E. P. J., eds, NATO Advanced Study Institute (ASI) Series C Vol. 262, Timing Neutron Stars. p. 27, doi:10.1007/978-94-009-2273-0_3

APPENDIX A: SOME EXTRA MATERIALS

This paper has been typeset from a $\text{\TeX}/\text{\LaTeX}$ file prepared by the author.

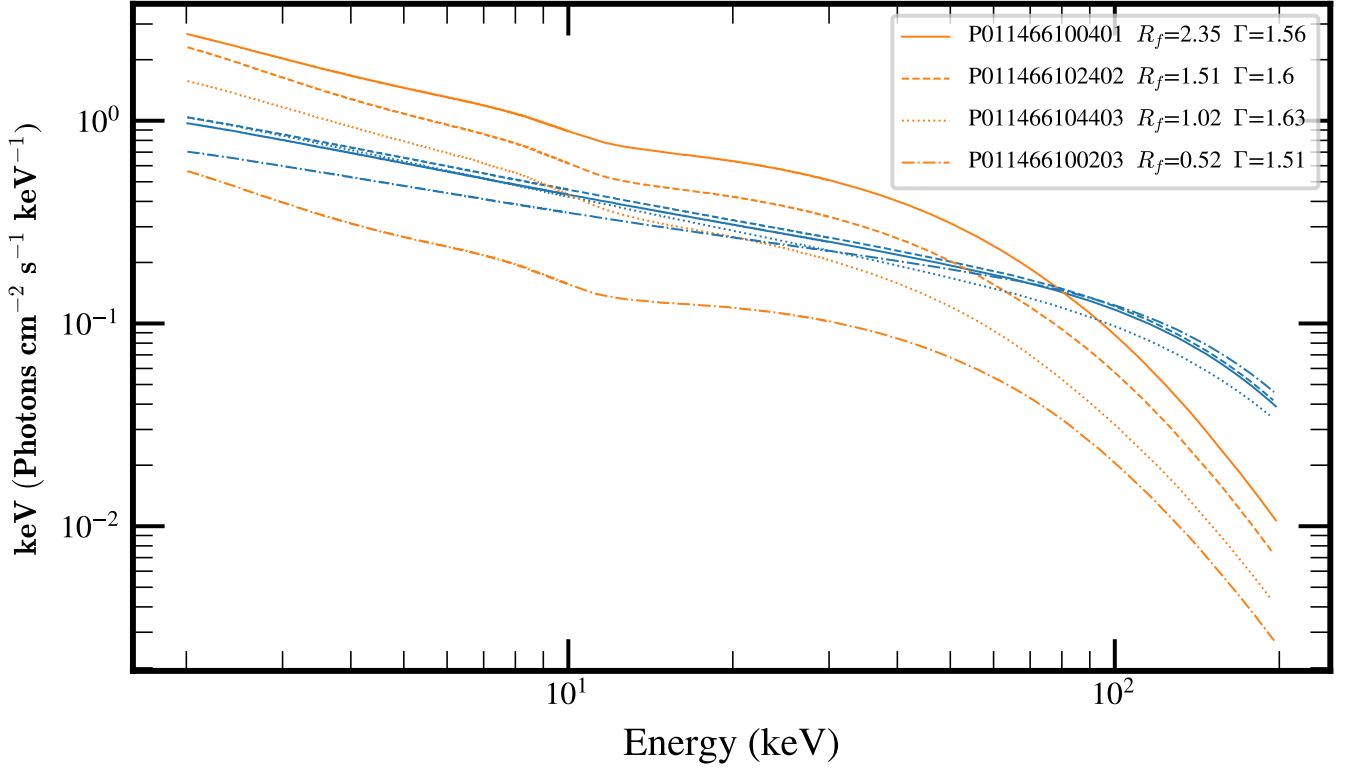


Figure A1. The corresponding Compton (in blue) and reflection (in orange) components of the best-fitting models under different reflection fractions R_f in *Insight*-HXMT observations. The exposure ID, R_f and Γ are present on the upper right in the figure. P011466100401, P011466102402 and P011466104403 are selected from the plateau phase of hard state that have similar L_C .

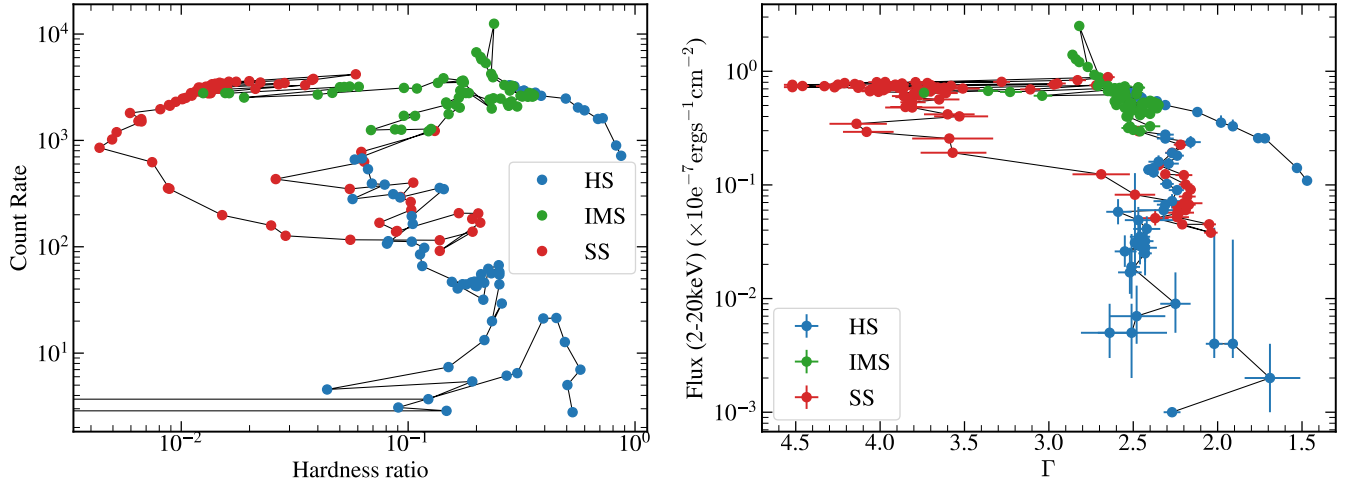
Table A1. The QPO information of each segment in *NICER* obsID 1200120196 and 1200120197

Start (s)	End (s)	Time (MJD)	$\nu_{C,QPO}$ (Hz)	$RMS_{C,QPO}$	$Q_{C,QPO}$	$\sigma_{C,QPO}$	$\nu_{B,QPO}$ (Hz)	$RMS_{B,QPO}$	$Q_{B,QPO}$	$\sigma_{B,QPO}$
142237907	142238873	58304.2728	$2.1063^{+0.0197}_{-0.0180}$	$0.0366^{+0.0017}_{-0.0018}$	5.6347	10.314	--	--	--	--
142269824	142271003	58304.6423	$2.9366^{+0.0201}_{-0.0208}$	$0.0277^{+0.0011}_{-0.0011}$	7.2508	12.419	--	--	--	--
142275663	142276722	58304.7098	$3.2084^{+0.0194}_{-0.0198}$	$0.0288^{+0.0008}_{-0.0011}$	6.0187	13.3546	--	--	--	--
142292969	142294468	58304.9101	$3.8371^{+0.0361}_{-0.0368}$	$0.0217^{+0.0012}_{-0.0012}$	6.05	8.7983	--	--	--	--
142298630	142300026	58304.9757	$4.2509^{+0.0225}_{-0.0268}$	$0.0206^{+0.0008}_{-0.0008}$	8.514	12.8107	--	--	--	--
142308700	142314902	58305.0922	$4.9658^{+0.0324}_{-0.0344}$	$0.0161^{+0.0009}_{-0.0009}$	7.7465	8.8628	--	--	--	--
142319818	142333386	58305.2209	$5.9361^{+0.0284}_{-0.0248}$	$0.0138^{+0.0004}_{-0.0004}$	4.9696	18.6406	$3.9725^{+0.1147}_{-0.1200}$	$0.0086^{+0.0004}_{-0.0003}$	2.7874	13.0669
142336496	142344002	58305.4139	$6.5140^{+0.0347}_{-0.0367}$	$0.0099^{+0.0003}_{-0.0003}$	7.3527	14.2943	$4.4448^{+0.1583}_{-0.1605}$	$0.0078^{+0.0004}_{-0.0004}$	3.2001	10.0584
142347614	142350064	58305.5426	$7.1084^{+0.0953}_{-0.0904}$	$0.0106^{+0.0007}_{-0.0007}$	3.3794	8.0053	$4.7946^{+0.1202}_{-0.1442}$	$0.0070^{+0.0005}_{-0.0005}$	5.542	6.8117
142353173	142355624	58305.6069	$8.0492^{+0.1531}_{-0.1288}$	$0.0051^{+0.0007}_{-0.0007}$	4.4178	3.4635	--	--	--	--
142358915	142383043	58305.6734	--	--	--	--	$4.1896^{+0.0450}_{-0.0420}$	$0.0077^{+0.0003}_{-0.0003}$	5.6398	12.8465

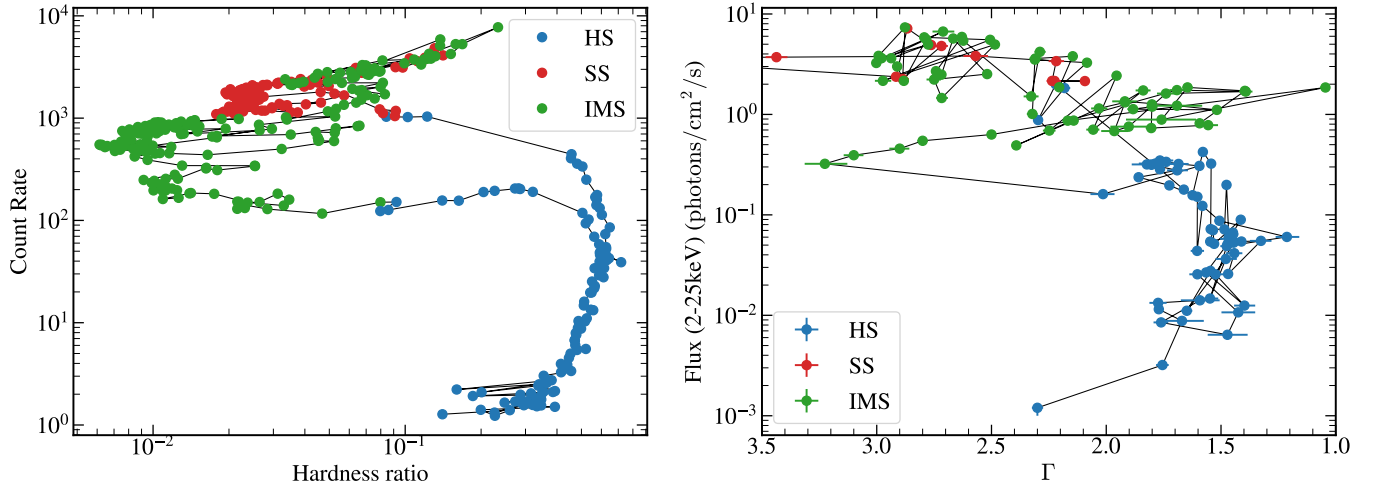
Notes:

Start: the start time of segments; End: the end time of segments; ν : centroid frequency; RMS: root mean square; Q: quality factor; σ : significance. The subscript B and C represent the type-B and type-C QPOs.

XTE J1550–564



GRO J1655–40



H1743–322

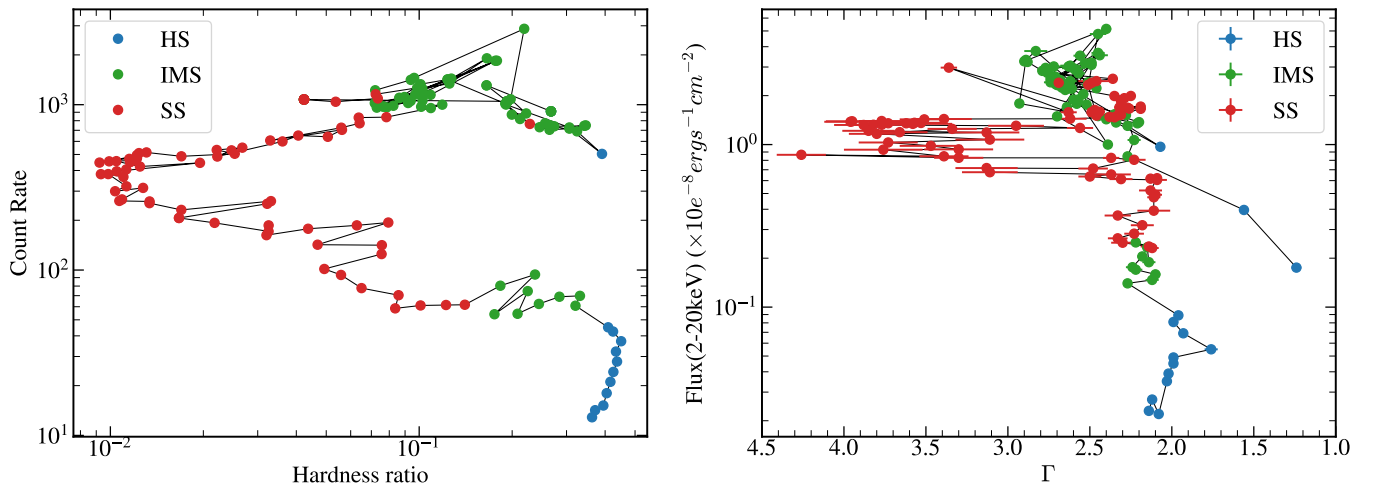


Figure A2. The hardness-intensity diagram (HID) and flux- Γ plane during three outbursts in other sources, with the left panels showing the HID and the right panels showing the flux- Γ plane. The outbursts, in order from top to bottom, are as follows: the 1998 outburst of XTE J1550–564, the 2005 outburst of GRO J1655–40 and the 2003 outburst of H1743–322. The HIDs are defined as the total 2.5–30 keV count rate vs. the ratio of hard (10–30 keV) to soft (2.5–6 keV) count rates from *RXTE/PCA*. The flux and Γ data are from public data in [Sobczak et al. \(2000\)](#); [Debnath et al. \(2008\)](#); [McClintock et al. \(2009\)](#), respectively.